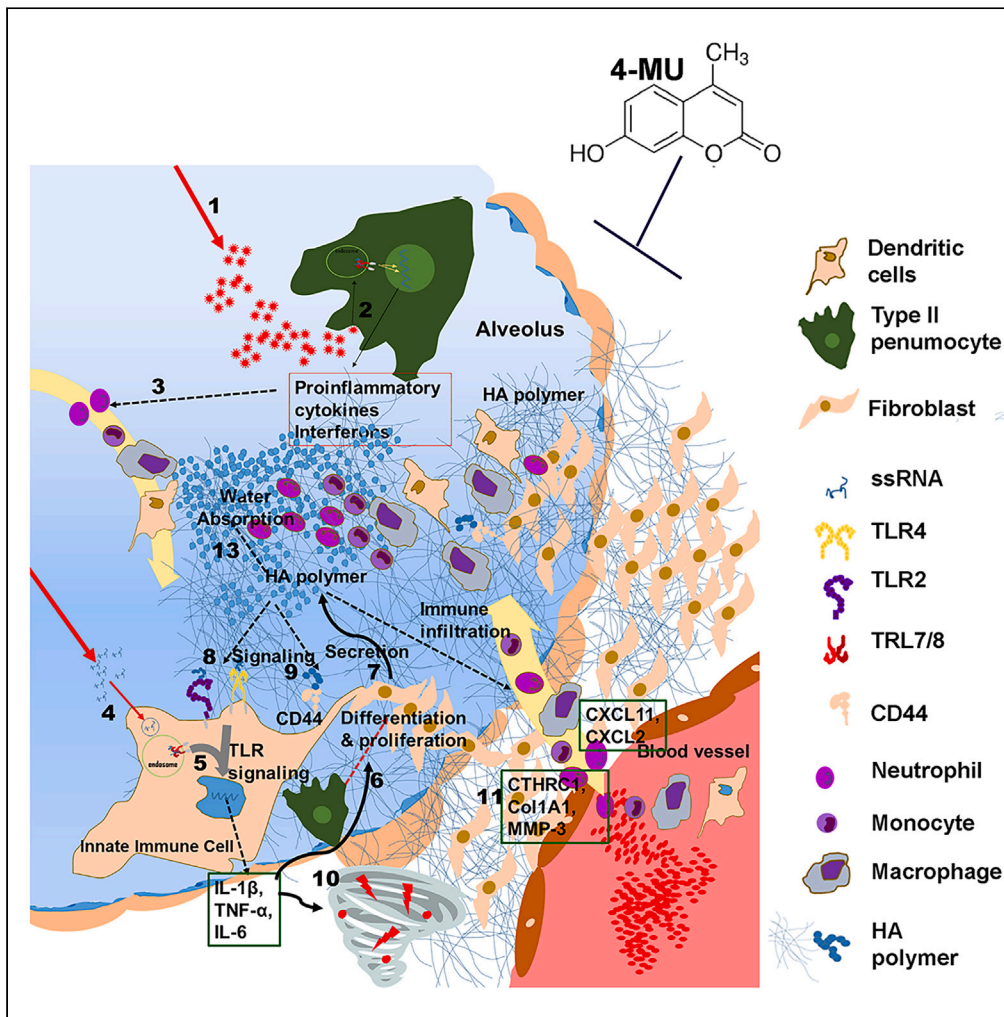Article

Simple virus-free mouse models of COVID-19 pathologies and oral therapeutic intervention

Huabin Zhu, Anuj K. Sharma, Karina Aguilar, ..., Bal L. Lokeshwar, Nagendra Singh, Vinata B. Lokeshwar

nasingh@augusta.edu (N.S.)
vlokeshwar@augusta.edu (V.B.L.)

Highlights

Simple virus-free models that mirror COVID-19 lung pathologies and severe morbidity

Adaptable COVID-19 mouse models to test Variants-of-concern or other RNA-virus illnesses

Hyaluronic acid as a critical mediator, if not as a driver of COVID-19 pathologies

Over-the-counter drug 4-methylumbelliferone as a potential treatment for COVID-19

Article

Simple virus-free mouse models of COVID-19 pathologies and oral therapeutic intervention

Huabin Zhu,[1,7] Anuj K. Sharma,[1,7] Karina Aguilar,[1,7] Faizan Boghani,[1] Semih Sarcan,[1] Michelle George,[1] Janavi Ramesh,[1] Joshua Van Der Eerden,[1] Chandramukhi S. Panda,[1] Aileen Lopez,[2] Wenbo Zhi,[3] Roni Bollag,[4,5] Nikhil Patel,[4] Kandace Klein,[6] Joe White,[4] Muthusamy Thangaraju,[1] Bal L. Lokeshwar,[5] Nagendra Singh,[1,*] and Vinata B. Lokeshwar[1,8,*]

SUMMARY

The paucity of preclinical models that recapitulate COVID-19 pathology without requiring SARS-COV-2 adaptation and humanized/transgenic mice limits research into new therapeutics against the frequently emerging variants-of-concern. We developed virus-free models by C57BL/6 mice receiving oropharyngeal instillations of a SARS-COV-2 ribo-oligonucleotide common in all variants or specific to Delta/Omicron variants, concurrently with low-dose bleomycin. Mice developed COVID-19-like lung pathologies including ground-glass opacities, interstitial fibrosis, congested alveoli, and became moribund. Lung tissues from these mice and bronchoalveolar lavage and lung tissues from patients with COVID-19 showed elevated levels of hyaluronic acid (HA), HA-family members, an inflammatory signature, and immune cell infiltration. 4-methylumbelliferone (4-MU), an oral drug for biliary-spasm treatment, inhibits HA-synthesis. At the human equivalent dose, 4-MU prevented/inhibited COVID-19-like pathologies and long-term morbidity; 4-MU and metabolites accumulated in mice lungs. Therefore, these versatile SARS-COV-2 ribo-oligonucleotide oropharyngeal models recapitulate COVID-19 pathology, with HA as its critical mediator and 4-MU as a potential therapeutic for COVID-19.

INTRODUCTION

The world-wide vaccination efforts against Severe Acute Respiratory Syndrome Coronavirus 2 (SARS-COV-2) have significantly reduced the frequency of hospitalizations for patients with COVID-19. Several therapeutics including oral antivirals, monoclonal antibodies, steroids, JAK-1/JAK-2 inhibitor, and anticoagulants also aid in preventing/reducing severe symptoms.[1,2] However, due to frequently emerging "variants-of-concern" (VOCs), COVID-19 infections are achieving a "seasonal" status such as the Influenza infections and will require newer vaccines and therapeutics for prevention and treatment.[3-5] A significant challenge for developing newer treatments and vaccines is the availability of preclinical models that reproducibly recapitulate the disease process without requiring live viral infections and accommodate testing of specific mutations that are present in the VOCs.

The current mouse models of SARS-COV-2 infection recapitulate many of the COVID-19 associated pathologies and symptoms, including acute inflammatory/immune response, cytokine storm, ground glass opacities, pulmonary fibrosis, acute respiratory distress syndrome (ARDS) and post-acute sequelae (PAC) or long-COVID.[6-10] However, due to the differences in the amino acid composition of the angiotensin converting enzyme −2 receptor between humans and mice, live virus infections require either humanized or transgenic mice, and viral strains adapted to infect mice.[6-10] A simple model that uses common mice strains and does not require adaptation would have the advantage of rapidly testing new treatments and preventive strategies against known and emergent VOC.

Hyaluronic acid (HA) is a major culprit in inflammatory lung diseases, including chronic obstructive lung disease (COPD), ARDS, asthma, and possibly COVID-19.[11-13] It is a non-sulfated glycosaminoglycan made up of repeated disaccharide units, N-acetyl-D-glucosamine, and D-glucuronic acid. In tissues, HA regulates hydration and osmotic balance, cellular functions, and immune cell infiltration.[14,15] Three HA-synthases (HAS1, HAS2, and HAS3) can synthesize HA, but the size of the HA polymer dictates its functions. In healthy lungs, HA is synthesized by type II alveolar and other types of cells but the basal HA levels are low.[14,15] During inflammation, HA levels are elevated by several fold due to

---

[1]Department of Biochemistry and Molecular Biology, Medical College of Georgia, Augusta University, 1410 Laney Walker Boulevard, Augusta, GA 30912, USA
[2]Clinical Trials Office, Augusta University, 1521 Pope Avenue, Augusta, GA 30912, USA
[3]Department of Obstetrics and Gynecology, Medical College of Georgia, Augusta University, 1410 Laney Walker Boulevard, Augusta, GA 30912, USA
[4]Department of Pathology and Biorepository Alliance of Georgia, Medical College of Georgia, Augusta University, 1120 15th St, Augusta, GA 30912, USA
[5]Georgia Cancer Center, Medical College of Georgia, Augusta University, 1410 Laney Walker Boulevard, Augusta, GA 30912, USA
[6]Department of Radiology and Imaging, Medical College of Georgia, Augusta University, 1120 15th Street, Augusta, GA 30912, USA
[7]These authors contributed equally
[8]Lead contact
*Correspondence: nasingh@augusta.edu (N.S.), vlokeshwar@augusta.edu (V.B.L.)
https://doi.org/10.1016/j.isci.2024.109191

the upregulation of HAS2 and to some extent HAS3 expression in alveolar cells. Subsequently, HA may be degraded by hyaluronidases and inflammation-associated reactive oxygen species to polymers of ≤ 500 kD.[13] CD44 is the major HA cell surface receptor expressed on all immune cell types.[13,16] By binding to CD44 and Toll-like receptors (TLRs) 2 and 4, HA induces inflammatory cytokine (e.g., IL-1β, TNF-α, and IL-6) production, which stimulates the infiltration of inflammatory cells. Therefore, HA promotes an inflammatory tissue microenvironment.[13,17,18] A study reported 24–27 non-coding RNA sequences in the SARS-COV-2 genome ("Human Identical Sequences") that apparently induce HAS2 expression; however, the mechanism remains unclear.[19]

4-methylumbelliferone (4-MU; 7-hydroxy-4-methylcoumarin), also known as Hymecromone, is an over-the-counter drug approved in Europe as a treatment for biliary spasms. 4-MU inhibits HA synthesis by competitively depleting UDP-glucuronic acid levels, and by downregulating HAS2 and HAS3 expression.[20–22] 4-MU has an excellent safety profile for humans and mice. The 50% toxic dose for 4-MU (Pubchem; compound CID 5280567) for mice and rats ranges between 2.8 g and >10 g per kg. Studies from our group and others have used 250 mg–1000 mg/kg dose to control tumor growth and metastasis in various mouse models.[23–25] 4-MU suppresses lung inflammation and neutrophil infiltration in murine models.[26,27] In human studies that include double-blinded placebo-controlled trials, the safety of oral 4-MU has been established at 2400 mg/day for up to 3 months, as a choleretic drug.[22] A U.S. based study showed that in healthy human volunteers, 4-MU oral dose up to 3600 mg/day was well tolerated; the reported mild to moderate adverse events (headache, gastrointestinal, and insomnia) resolved without intervention.[28]

There were two main objectives of this study. First was to generate a mouse SARS-COV-2 model that does not require a live virus infection, is adaptable for any SARS-COV-2 variant and recapitulates the COVID-19 lung pathologies. The second objective was to evaluate if HA is a major component of the SARS-COV-2 associated lung pathologies both in human disease and mouse models. Furthermore, at the human equivalent dose, if 4-MU abrogates COVID-19 pathologies and associated morbidity in the treatment, prevention, and long-term outcome setting.

RESULTS

Oropharyngeal model for COVID-like pathology

Toll-like receptors (TLRs) 7 and TLR8 are the natural receptors for uridine-rich single stranded RNA (ssRNA). GU-rich sequences from RNA viruses such as human immunodeficiency virus and SARS-COV-1 bind TLR7/8 and induce signaling.[29,30] We identified a GU-rich sequence in the SARS-COV-2 genome that is present in all known COVID-19 variants (CV2; key resources table). This sequence met the selection criteria of >40% content of GU or UG pairs and at least one GUGU or UGUG motif.[29,30] We assessed the binding efficiency of CV2 to mouse and human TLR protein sequences using the Random Forest classifier.[31] The classifier predicted the strongest binding efficiency of CV2 to Tlr7 (mouse) and TLR7 (human) proteins, followed by TLR-8 (Table S1). We synthesized the CV2 ribo-oligonucleotide with a thioester bond to increase stability (key resources table). We delivered CV2 either alone or with low dose bleomycin (BE) through the oropharyngeal route once daily for seven days, to mimic sustained SARS-COV-2 infection. BE is known to cause lung fibrosis when administered by intratracheal or oropharyngeal route.[32–34] The oropharyngeal (OP) model was based on a method described by Egger et al.[35] We used an 8- to 10-fold lower dose of BE (0.125 mg/kg) to facilitate inflammation without causing lung fibrosis. Magnetic resonance imaging (MRI) on day ten showed subtle scattered areas of increased signal and a small unilateral pleural effusion in the lungs of mice receiving CV2 alone and minimal changes in the BE alone group (Figure 1A). Contrarily, mice receiving BE + CV2 OP instillations showed hypertensive signal affecting both lobes, representative of ground glass opacities with some showing consolidative opacities (Figure 1A). The MRI signal volume was ≥ 4-fold higher in the BE + CV2 group compared to the control, BE and CV2 groups (Figure 1B). Mice in the BE + CV2 group also lost 15% of body weight by day 10, an experimental endpoint as per the institutional guidelines (Figure 1C).

Lung pathology in the BE + CV2 group showed bronchiolar epithelial cells with reactive atypia and cytopathic effects resembling a viral infection, (Figure 1D). Interstitial fibrosis was also evident along with the loss of alveolar space, and the inflammatory infiltrates comprising of macrophages, and lymphocytes were more pronounced around the bronchioles. The lungs did not show eosinophilia, granuloma, or fibrotic foci; the latter is a characteristic of an interstitial lung disease. Ground glass opacities, loss of alveolar space, interstitial fibrosis, and immune infiltrates are the hallmarks of COVID-19 induced lung pathology.[36,37]

4-methylumbelliferone prevents the development of COVID-19-like lung pathology

The ground glass opacities reported in the lungs of patients with COVID-19 and in BE + CV2-treated mice are consistent with the gel-like properties of HA.[14,15] Therefore, we determined if 4-MU has therapeutic efficacy in the BE + CV2 OP model at 250 mg/kg dose which is (human equivalent dose, 1400 mg/day/70kg). In clinical studies, 4-MU has been tried at 2- to 3-fold higher doses.[22,38] Mice receiving a daily gavage of 4-MU starting on the day of BE + CV2 OP instillation, did not develop ground glass or consolidative opacities (Figure 1A). MRI signal intensities in the 4-MU treatment group were not significantly different from the normal control group (Figure 1B). Moreover, mice in the 4-MU treatment group maintained a stable weight (Figure 1C). Histopathology showed normal alveolar architecture in >80% areas of the lungs in 4-MU treated mice, with the remaining 20% areas showing a resolving infection (Figure 1D).

Pharmacokinetics of 4-methylumbelliferone in lung tissues

In the liver, 4-MU is metabolized into two major metabolites, 4-MU sulfate (4-MUS) and 4-MU glucuronide (4-MUG) with futile cycling between 4-MU and the metabolites.[39] 4-MUG is a stable metabolite which also inhibits HA synthesis.[38] Following a single oral dose of
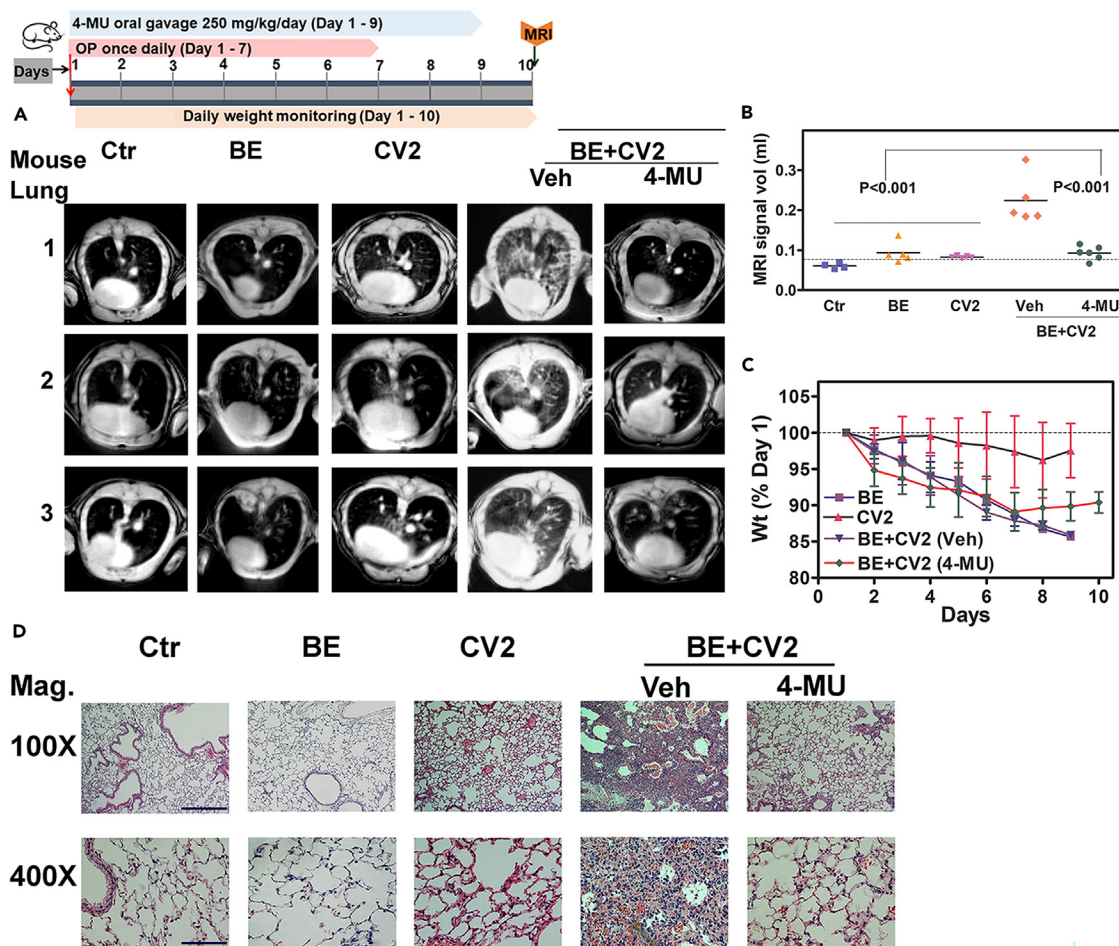
Figure 1. Evaluation of lung pathology in the OP model and its prevention by 4-MU oral treatment

As shown in the schematic, C57BL/6 mice received the oropharyngeal instillation of BE, CV2 or BE + CV2. Concurrently, mice in the BE + CV2 group were treated once daily with vehicle or 4-MU oral gavage until day 9. Mice were imaged by MRI on day ten, which was the experimental endpoint. Number of mice in each group: Control (ctr) n = 4; BE, CV2, BE + CV2, Vehicle (Veh): n = 5; BE + CV2 (4-MU), n = 6. The experimental endpoint was day ten, as the mice in the BE + CV2 vehicle group became moribund and showed about 15% loss of body weight.

(A) MRI images of the lungs from three representative mice in each group on day ten.

(B) Quantification of the MRI signal in the lungs on day 10. Dots represent MRI signal data for individual mice in each group; the line shows the mean intensity in each group.

(C) Body weights of mice in each group. The Y axis shows the percentage of mice weights compared to day 1 (100%) in each group. The experimental endpoint was based on the drop in body weight by 15% in the vehicle group. Data in B and C: Mean $\pm$ SD.

(D) Representative hematoxylin-Eosin images of lung tissues in different groups at endpoint (day 10).

4-MU (250 mg/kg), while 4-MU and its metabolites were rapidly cleared from the lung tissues, we observed a second peak for both 4-MUS and 4-MUG at 8 h (Figure 2A). 4-MUG was the major metabolite and its concentration exceeded 2 mg/g of lung tissue at 8 h; even at 12 h, 4-MUG levels were 0.32 mg/g (Figure 2A). These levels were significantly higher than the IC_{50} of HA synthesis.

Increased hyaluronic acid and hyaluronic acid family expression in the BE + CV2 oropharyngeal model and its attenuation by 4-methylumbelliferone

We measured HA levels in lung tissue extracts of mice from the control group and from BE + CV2 groups treated with either vehicle or 4-MU (as described in Figure 1). HA levels measured by the HA test,[40,41] detected minimal basal HA levels in the control mice. However, HA levels were 7-fold elevated in the vehicle treated group (Figure 2B). In the 4-MU treatment group, HA levels were comparable to the basal HA levels (Figure 2B). Among the HA synthases, HAS1 and HAS3 protein expression was low in mice lungs (Figure 2C). However, the expression of HAS2, CD44, and collagen type 1A1 (Col1A1) proteins was elevated in the lung extracts of mice from the BE + CV2 vehicle group (Figure 2C; Table S2). We have shown that CD44-HA interaction induces CD44 expression through autocrine signaling.[24,25] Similarly, HA induces Col1A1
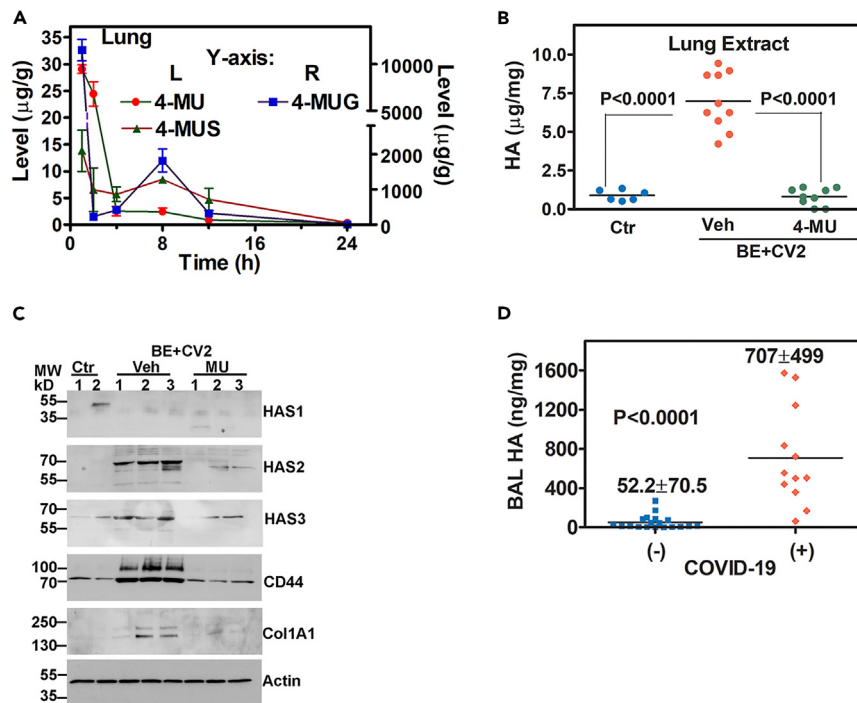
Figure 2. Pharmacokinetics of 4-MU and the measurement of HA, HA-family molecules in the lung and BAL specimens

(A) Pharmacokinetics of 4-MU. Levels of 4-MU, 4-MUS and 4-MUG were measured by LC-MRM-MS in lung tissues at different times following oral gavage. Multiple transitions (parent ion/daughter ion pairs) were monitoring for each drug and the ones used for quantification (quantifier) were 175.1/133.0, 351.0/175.1 and 255.0/175.1 for 4-MU, 4-MUG and 4-MUS, respectively. The integrated peak areas for these transitions were calculated for each sample using the Skyline software (version 20.0, University of Washington). Data: Mean ± SD (n = 3).

(B) HA levels in lung tissue extracts from mice in the control, vehicle and 4-MU treatment groups (described in Figure 1) were measured by the HA test and normalized to total protein. Data: Mean ± SD HA levels (μg/mg protein) in mouse tissue extracts (n = 3).

(C) Immunoblot analysis of mice lung extracts from various groups (described in Figure 1), for HA-family and Col1A1 proteins; actin is the loading control.

(D) HA levels measured in BAL specimens from patients with COVID-19 (+); n = 12 or other respiratory or cardiovascular pathologies (−); n = 19. Dots represent HA levels in individual patients; the line indicates mean HA levels in each group.

expression which is known to promote fibrosis.[42] HAS2, CD44, and Col1A1 levels in the 4-MU treatment and control groups were similar (Figure 2C; Table S2).

Hyaluronic acid/hyaluronic acid family expression in the BE + CV2 oropharyngeal model mirrors human COVID-19 lung pathology

Since HA levels were elevated in lung extracts from the vehicle group of the BE + CV2 OP model, we measured HA levels in bronchoalveolar lavage (BAL) specimens from patients with COVID-19 and other conditions that required intubation (n = 31; Table S3). Compared to the patients with other lung pathologies (e.g., COPD, pneumonia, and so forth), HA levels were elevated 13.6-fold in BAL specimens from patients with COVID-19 (Figure 2D). In univariate analysis, COVID-19 status significantly correlated with HA levels but not with race, sex, or mortality (Table S4). Elevated HA levels had 83% sensitivity and 100% specificity to associate with COVID-19 diagnosis (Table S4).

In a second cohort, we stained lung specimens obtained at autopsy from patients with COVID-19 and other causes, for HA, HAS2, CD44, and Col1A1 by immunohistochemistry[25,43] (Table S5). In parallel, we stained lung specimens from mice in the control, and OP model groups for the same markers. Compared to COVID-19 negative (−) pathologies, HA, HAS2, CD44, and Col1A1 expression were 3- to 7-fold elevated in lung specimens from patients with COVID-19 (Figures 3A and 3C). While HA and Col1A1 formed a dense extracellular matrix surrounding the thickened alveolar epithelium with reduced alveolar spaces, HAS2, and CD44 were expressed in both epithelial and stromal cells (Figure 3A). Mirroring this pattern, lung specimens from the BE + CV2 vehicle group showed a 10- to 20-fold higher expression of HA, HAS2, CD44 and Col1A1, which was significantly reduced in the 4-MU treatment group (Figures 3B and S1).

4-methylumbelliferone inhibits an inflammatory signature in the BE + CV2 oropharyngeal model

Given the pivotal role of HA in inflammation and inflammation being a prime factor in COVID-19 pathology, we evaluated the expression of ten transcripts, associated with inflammation, the cytokine storm and immune cell infiltration: HAS2, CD44, Col1A1, MMP-3, CTHRC1, IL-1β,
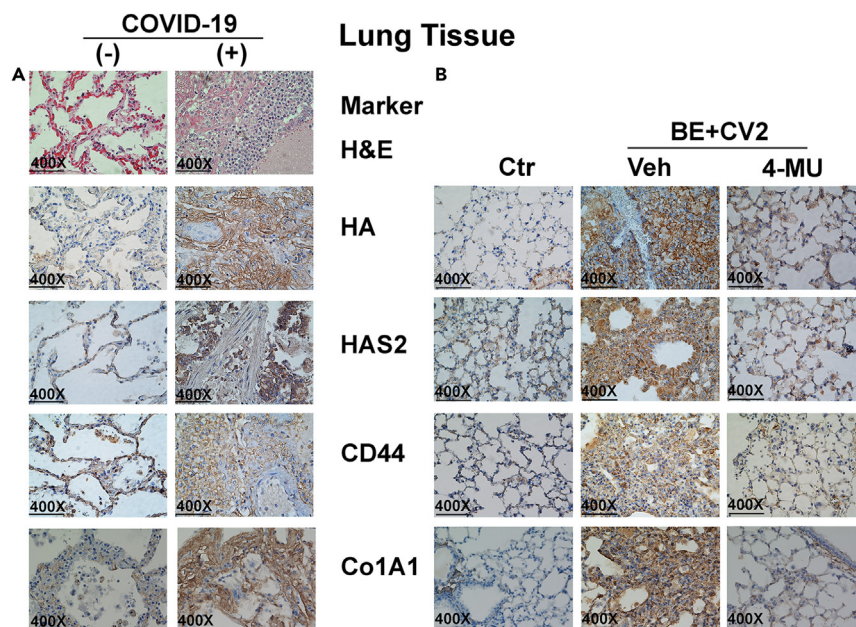
Figure 3. Immunohistochemical analyses of human and mouse lung tissues for HA, HA-family and Col1A1

(A–C) HA, HAS2, CD44 and Col1A1 were localized by IHC in human lung tissues from patients with (+) or without (−) COVID-19 and in mouse lung tissues from the control, and BE + CV2 (vehicle, 4-MU) groups described in Figure 1. Representative specimens from each category are shown. (A) H&E and IHC staining images of human lung tissues. (B) Mouse lung IHC images. Note, H&E images for mouse tissues are shown in Figure 1C. The quantification of staining intensities is shown in Figure S1.

TNF-α, IL-6, CXCL1, and CXCL2.[44–50] The expression of all the ten transcripts was measured using a reverse transcription polymerase chain reaction using gene specific primers[25,43,51] (Table S6). The expression of various transcripts was 3- to ≥10-fold elevated in the vehicle group, as compared to the control and 4-MU treatment groups (Figures 4A–4J). Hierarchical clustering of the transcript data was performed using the heatmapper software,[52] and showed an overall grouping of specimens in the control, vehicle, and 4-MU treatment groups, suggesting that these ten transcripts likely represent a signature for the COVID-19-associated lung pathology and its resolution by 4-MU treatment (Figure 4K).

Immune cell infiltration in the BE + CV2 oropharyngeal model mimics human COVID-19 pathology and is inhibited by 4-methylumbelliferone

Increased infiltration of macrophages (CD68+), T-cells (CD3+) and neutrophils is commonly observed in lung specimens of patients with COVID-19.[53–55] IHC of the postmortem lung specimens from patients with COVID-19 showed 5- to 9-fold higher infiltration of myeloid linkage cells (i.e., CD68+ monocyte/macrophages), T-cells (CD3+) and neutrophils (myeloperoxidase [MPO]+) compared to patients with other respiratory or cardiac events (Figures 5A and S2). Lung specimens of mice in the vehicle group (BE + CV2 OP model) showed 4- to 8-fold higher infiltration of macrophages, T-cells, and neutrophils (Ly6G+; Figures 5B and S2) than control mice. Furthermore, the increased infiltration was >90% inhibited in the 4-MU treatment group (Figures 5B and S2).

4-methylumbelliferone inhibits COVID-19 like lung pathology in a treatment setting

While 4-MU inhibited the development of lung pathology when administered concurrently with the BE + CV2 instillations, we next investigated if 4-MU has efficacy in treating an established/ongoing COVID-19 like pathology. In this setting, mice received OP installations of BE + CV2 for three days, followed by oral treatment with vehicle or 4-MU from day four to ten. MRI imaging on day four (before starting the 4-MU treatment) showed scattered areas of increased signal (Figure 6A). On day ten, mice in the vehicle treatment group showed a hyperintense signal involving bilateral lower lungs with ground glass opacities (Figure 6A). In the 4-MU treatment group, hyperintense signal was absent, and areas of increased signal that were detected on day four before starting the treatment had resolved (Figure 6A). The mean MRI signal volume was about 3-fold higher in the vehicle group compared to the 4-MU treatment group (Figure 6B).

The mice in the vehicle treatment group lost about 14% of body weight within ten days; however, the 4-MU treated group showed ≤5% weight loss (Figure 6C). Lung specimens from the vehicle group showed loss of alveolar space and interstitial fibrosis without significant eosinophilia or granuloma. The inflammatory component in the interstitium was filled with lymphoplasmacytic infiltrate. Furthermore, bronchial epithelial cells showed reactive atypia and giant multinucleated cells that are characteristic of viral cytopathic effects (Figure 6D). Contrarily,
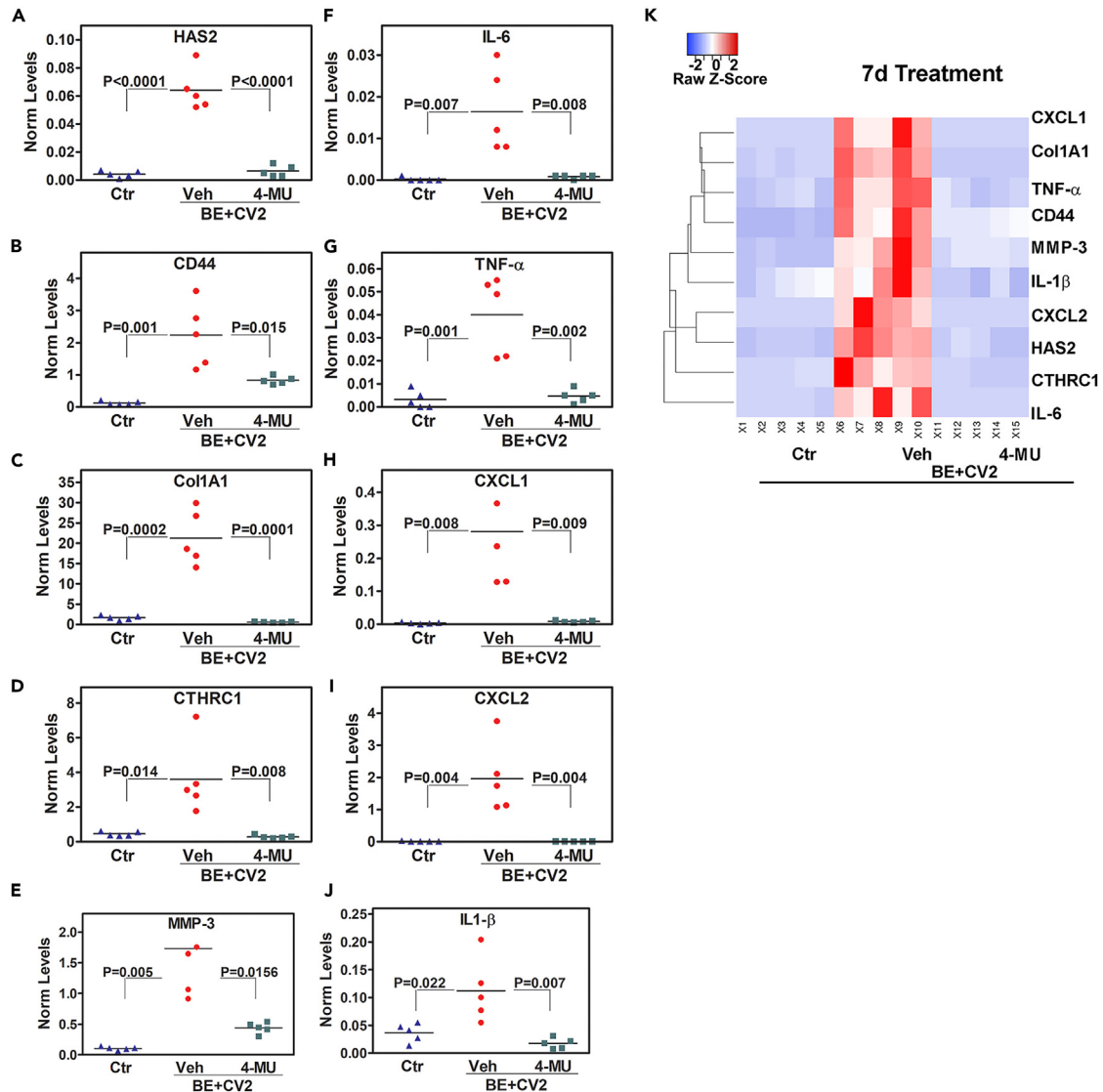
Figure 4. Evaluation of an inflammatory transcript signature in the BE + CV2 OP model

RT-qPCR analyses for a ten gene signature was peformed on RNA isolated from lung tissues of mice in the control or BE + CV2 groups (Vehicle or 4-MU). The BE + CV2 treatment groups are described in Figure 1. The levels of each transcript were measured in lung tissues collected on day ten (experimental endpoint).

(A–J) Panels show the levels of the indicated transcripts. Dots represent the levels of a particular transcript in individual tissues; the line shows mean transcript levels in each group (n = 5 per group).

(K) Hierarchical clustering of the transcript expression data shown in panels A – J.

lung specimens from the 4-MU treatment group showed normal alveolar architecture without interstitial fibrosis or lymphoplasmacytic infiltrate (Figure 6D).

The ten-transcript signature consisting of HAS2, CD44, Col1A1, CTHRC1, MMP-3, IL-1β, IL-6, TNF-α, CXCL1, and CXCL2 accurately clustered the specimens in the control, vehicle, and 4-MU treatment groups (Figure 6E). The levels of all ten transcripts were 10- to 20-fold elevated in the vehicle group compared to the control and the 4-MU treatment (Figure S3).

Hyaluronic acid matrix supports immune cell infiltration and its inhibition by 4-methylumbelliferone

During inflammation, the adhesive cables of HA matrix support immune cell migration.[56,57] We co-localized HA and individual immune cell types, i.e., CD68+ macrophages, CD3+ T-cells and MPO+ neutrophils in postmortem lung specimens from patients with or without COVID-19 pathology (Table S5). Lung specimens from patients with COVID-19 showed an increased number of macrophages, T-cells and neutrophils embedded within the HA matrix. Contrarily, lung specimens from patients who died of other pulmonary and/or cardiovascular causes showed
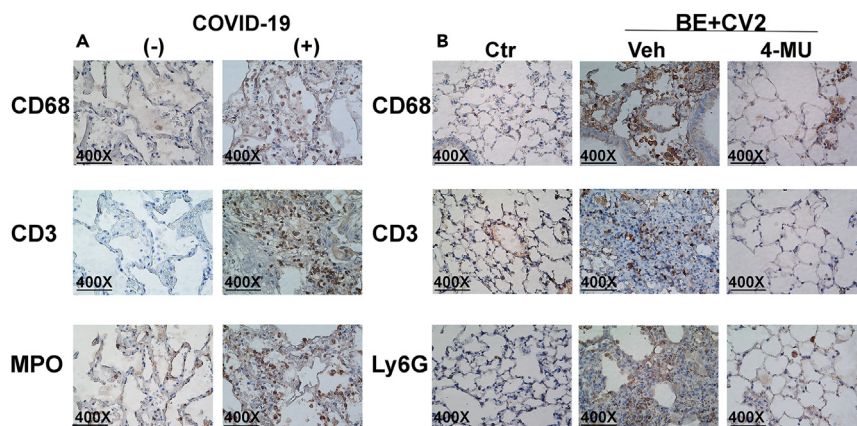
Figure 5. Immune cell expression in human and mouse lung tissues
Immune cells i.e., macrophages (CD68$^+$), T-cells (CD3$^+$) and neutrophils (MPO for human; Ly6G for mouse) were analyzed in human and mouse lung tissues by IHC.
(A) Representative images of human lung tissues from patients with (+) or without (−) COVID-19 showing the infiltration of specific immune cell types.
(B) Representative images showing indicated immune cell infiltration in mice lungs from the control, and BE + CV2 instillation groups (vehicle and 4-MU treatment). The quantification of staining intensities is shown in Figure S2.

less deposition of HA matrix and immune cell infiltration (Figures 7A, 7C, and S4–S6). Lung specimens from control mice showed minimal HA matrix and immune cell infiltration (Figures 7B, 7C, and S4–S6). However, mice lungs in the vehicle group from the three-day BE + CV2 OP model showed massive (6- to 20-fold) infiltration of macrophages, T-cells and neutrophils embedded in a dense HA matrix (Figures 7B, 7C, and S4–S6). The HA matrix in the lungs of mice from the 4-MU treatment group was sparse with a concomitant 4- to 10-fold reduction in immune cell infiltration (Figures 7B, 7C, and S4–S6).

4-methylumbelliferone treatment has efficacy in the long-term recovery of COVID-19 like effects

The data presented in Figures 1 and 6 shown that 4-MU is effective in the prevention and treatment settings. Therefore, we examined if 4-MU treatment could have efficacy in the long-term recovery even after a severe infection, we performed OP instillations of BE + CV2 for seven days and the mice were treated with 4-MU or vehicle from days four to fifty. In this setting, 66% of the mice recovered based on MRI imaging and after losing about 14% of their body weight by day ten, the surviving mice gained weight to the pre-BE+CV2 instillation level (Figures S7A–S7C). The mice that recovered showed normal lung architecture with minimal areas of interstitial fibrosis or immune cell infiltration (Figure S7D).

4-methylumbelliferone effectively inhibits severe COVID-19 like pathology in the BE + Delta/Omicron (Δ/O) ribo-oligonucleotide oropharyngeal model

SARS-COV-2 variants such as Delta (Δ) and Omicron (O) contain multiple mutations, including the L452R mutation that likely increases the evasion of the immune system, and viral transmissibility. Curiously, this mutation is within a GU/UG rich sequence. We evaluated if the COVID-19 like lung pathology could be induced by this GU/UG ribo-oligonucleotide containing the L452R mutation (Δ/O). The RF classifier prediction showed that Δ/O can interact with both mouse and human TLR7 proteins with 75% efficiency. We delivered BE+(Δ/O) combination once daily for seven days. Concurrently, mice were treated with vehicle or 4-MU once daily from day one to nine. MRI imaging on day ten showed a bilateral hyperintense signal with areas representing ground glass opacity and more focal areas related to consolidative opacities. In the 4-MU treatment group, there was a significant decrease to the complete absence of hyperintense signal (Figure 8A). The mean MRI signal volume was about 2.5- to 3-fold higher in the vehicle group compared to the 4-MU treatment group (Figure 8B). Mice in the vehicle group showed about 15% weight loss, whereas the mean weight loss in the 4-MU treatment group was about 6% (Figure 8C).

Lung pathology in the vehicle group revealed cytopathic effects, interstitial fibrosis, loss of alveolar space, and infiltration of immune cells. Additionally, significant areas of the bronchioles were filled with mucus and neutrophilic debris. Consistent with the MRI findings, in the 4-MU treatment group, lung pathology showed normal alveolar architecture with minimal interstitial fibrosis or lymphoplasmacytic infiltrates in the interstitium (Figure 8D). The ten-transcript signature clustered the specimens into control, vehicle, and 4-MU treatment categories (Figure 8E). Quantitatively, the expression of all transcripts was 10- to 40-fold elevated in the vehicle group compared to the control and 4-MU treatment groups (Figure S8). The lung tissues from the vehicle group showed increased deposition of dense HA matrix with immune cell infiltration in (Figure S9). Like the control group, in the 4-MU treatment group, the HA matrix was sparse with minimal immune cell infiltration (Figure S9).
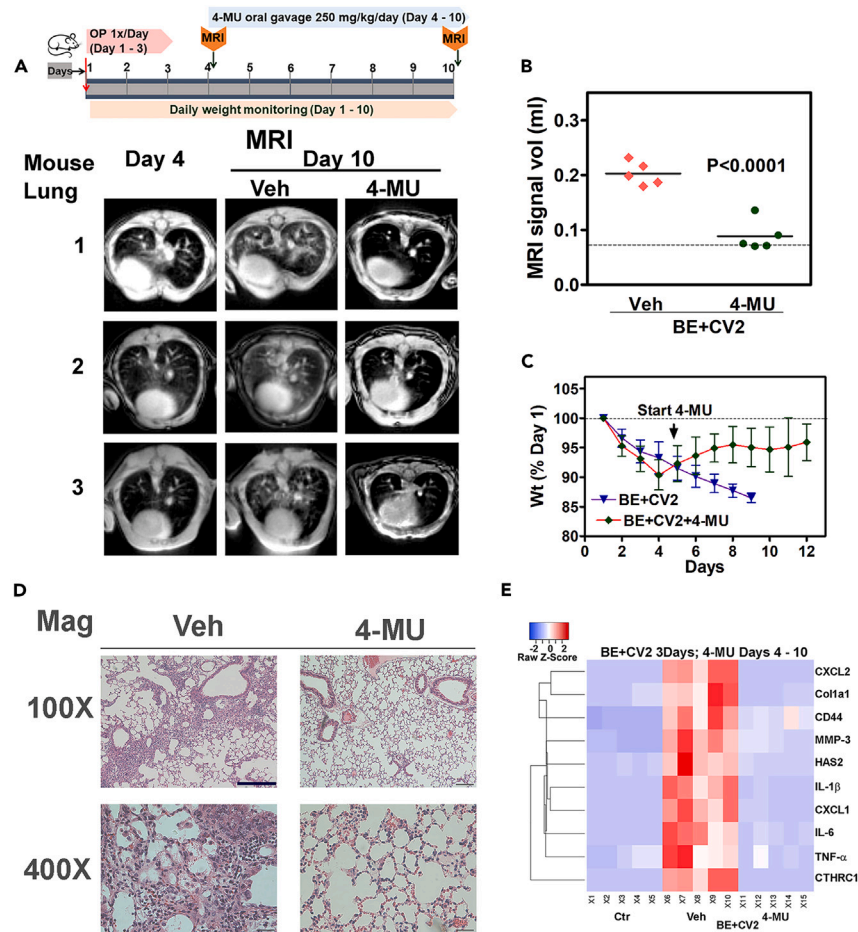
Figure 6. Evaluation of 4-MU treatment efficacy in the BE + CV2 OP model in an established/ongoing COVID-19 like pathology setting

As shown in the schematic, C57BL/6 mice received the oropharyngeal instillation of BE + CV2, once daily for three days. Mice were then treated once daily with vehicle or 4-MU oral gavage starting on day four until day ten (experimental endpoint); n = 5 per group. The experimental endpoint was day ten, as the mice in the BE + CV2 vehicle group became moribund and showed about 15% loss of body weight.

(A) MRI images of the lungs from three representative mice on day four (before starting 4-MU treatment) and on day ten.

(B) Quantification of the MRI signal from the lungs of mice in each group. Dots represent the MRI signal data for individual mice in each group; the line shows the mean intensity in each group.

(C) Body weights of mice in each group. The Y axis shows the percentage of mice weights compared to day 1 (100%) in each group. Data in B and C: Mean ± SD.

(D) Representative hematoxylin-Eosin images of lung tissues in different groups at endpoint (day 10).

(E) Hierarchical clustering of the expression of the ten transcripts in mouse tissues from the control, vehicle and 4-MU treatment groups. The transcript expression data are shown in Figure S3.

DISCUSSION

Our study reports three salient findings, which are schematically explained in Figure 9. First, this study describes virus-free BE + CV2 and BE+(Δ/O) models that mirror COVID-19 pathologies. Second, the study shows compelling evidence for HA as a mediator, if not as a driver of COVID-19 pathologies. Third, the study provides a strong rationale for the use of 4-MU in preventing and treating severe symptoms and plausibly PAC. The use of SARS-COV-2 ribo-oligonucleotides for inducing COVID-19 pathologies makes the model universally adaptable. The ribo-nucleotides can be inexpensively synthesized by any commercial vendor and the models can potentially test any "mutation of interest" in VOCs without needing viral adaptation to mice or creating a humanized mouse. Furthermore, BE + CV2 OP instillation models can be established in any laboratory world-wide, as they do not require BSL-3 facilities, which is necessary when using live SARS-COV-2.

In BE + CV2 and BE+(Δ/O) models, the amount, and duration of OP instillations of the ribo-oligonucleotides can be controlled to allow the testing of any drug in the prevention, therapeutic and PAC settings. In our study, daily instillations of BE + CV2 for seven days mirrored an active severe infection. An OP installation for three days, with treatment starting on day four, is like a clinical scenario where early symptoms trigger diagnostic testing and treatment after a positive test. Treatment of mice up to fifty days after OP instillations for seven days mirror testing treatment efficacy for PAC after a severe infection.
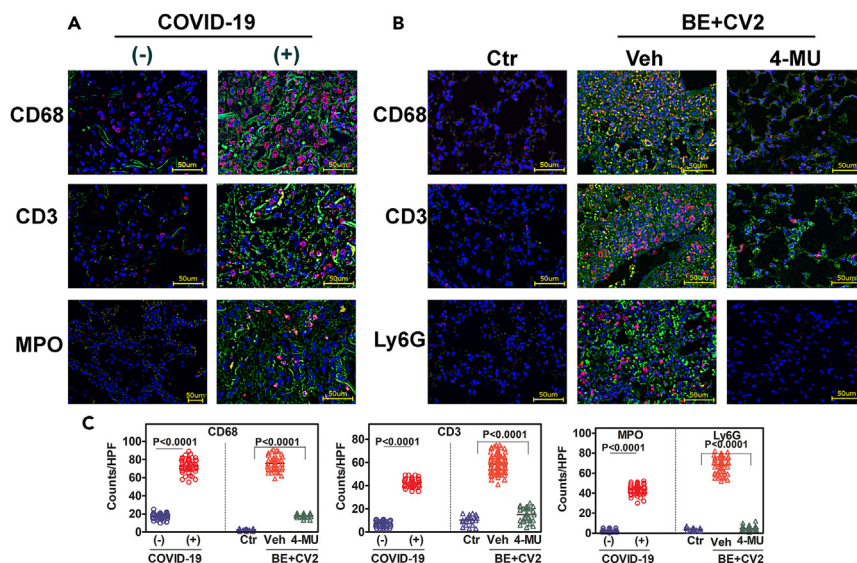
Figure 7. Localization of immune cells on HA matrix in human and mouse lung tissues

Lung tissues from patients and mice were stained simultaneously for HA and macrophages (CD68^{+}), T-cells (CD3^{+}) or neutrophils (MOP for human; Ly6G for mouse) by immunocytochemistry. Alexa Fluor 594 (red) represents immune cells; Alexa Fluor 488 (green) shows the HA matrix.

(A) Representative merged images of lung tissues from patients with (+) or without (−) COVID-19 showing the infiltration of specific immune cell types on the HA matrix.

(B) Representative images showing indicated immune cell infiltration in mice lungs from the control, and BE + CV2 instillation groups (vehicle and 4-MU treatment) described in Figure 6. For the merged images shown in panels A and B, images of the same tissues with each fluorophore and DAPI (nuclear staining) are shown in Figures S4–S6.

(C) Quantification of immune cell infiltration in human and mouse lung tissues. Dots represent counts per high power field. The line shows the mean number of immune cells infiltrated in a high power field (n = 15–50 HPF counts per group).

Both BE + CV2 and BE+(Δ/O) models display classic COVID-19 pathologies, including ground glass opacities, pulmonary fibrosis, loss of alveolar space, viral cytopathic effects and immune infiltrates consisting of macrophages/monocytes, T-cells, and neutrophils in lung tissues. Furthermore, the MRI findings and weight loss are comparable to the worsening of symptoms in the absence of treatment. Death as an endpoint could not be evaluated due to institutional guidelines for animal welfare. The models rely on low dose BE to facilitate lung injury/inflammation. However, unlike the BE-induced ARDS in other models,[58] BE alone at low dose did not induce lung pathologies.

In published studies, including one study that evaluated HA levels in the plasma of patients with COVID-19, HA levels are compared between healthy individuals and patients with lung pathologies.[13,14,19] However, plasma HA levels reflect inflammation in any organ of the body. In two independent patient cohorts, we found that HA levels were >10-fold elevated in BAL and lung specimens from patients with COVID-19 as compared to patients with other lung pathologies. Significantly higher HA levels in the lungs are likely to cause the massive accumulation of fluid and ground opacities observed in the COVID-19 infection. A concomitant increase in the expression of the HA family in lung specimens from patients with COVID-19 further confirms the role of HA as a significant mediator of severe COVID-19 pathologies.

The elevated ten-transcript inflammatory signature, consisting of HAS2, CD44, IL-1β, TNF-α, IL-6, Col1A1, CTHRC1, MMP-3, CXLC1, and CXCL2, is related to the role of HA in establishing COVID-19 pathology in the BE + CV2 and BE+(Δ/O) models. For example, HA induces the expression of pro-inflammatory cytokines IL-1β, TNF-α, and IL-6, which are part of the cytokine storm observed in COVID-19.[13,49,59] HA also induces the expression and deposition of Col1A1 and of a related molecule, Collagen Triple Helix Repeat Containing 1 protein (CTHRC1). Both Col1A1 and CTHRC1 are elevated in the lungs of patients with COVID-19.[46,47,50] IL-1β induces the expression of MMP-3, which is a potential biomarker and therapeutic target for COVID-19.[48,49] Neutrophilic inflammation is a hallmark of COVID-19 infection. Chemokines CXLC1 and CXCL2, which neutrophil recruitment at the site of inflammation, are upregulated in COVID-19.[53]

Innate and adaptive immunological responses in COVID-19 infections show peripheral blood abnormalities that include neutrophilia, lymphopenia, and atypical immune cells.[55] However, lung specimens from patients with COVID-19 have increased the infiltration of monocytes/macrophages, T-cells and neutrophils.[53,54] During inflammation, immune cell infiltration is supported by the rolling of immune cells on "HA cables" via cell-surface HA-CD44 interaction.[13] Our data on the co-localization of HA and individual immune cell types in lung specimens from patients with COVID-19 and mouse models provide direct evidence for the causative role of HA in recruiting immune cells to the lungs.

4-MU is the only well-characterized inhibitor of HA synthesis and has an excellent safety profile in human studies.[22,28] In the BE + CV2 and BE+(Δ/O) models, 4-MU treatment downregulated increased HA and HA family expression, inflammatory signature, and immune cell infiltration regardless of if 4-MU was administered concurrently will be + CV2 (or BE+(Δ/O)) OP instillations (i.e., prevention setting) or after the COVID-19 such as pathology was established (i.e., treatment setting). In both settings, 4-MU oral treatment prevented/inhibited the
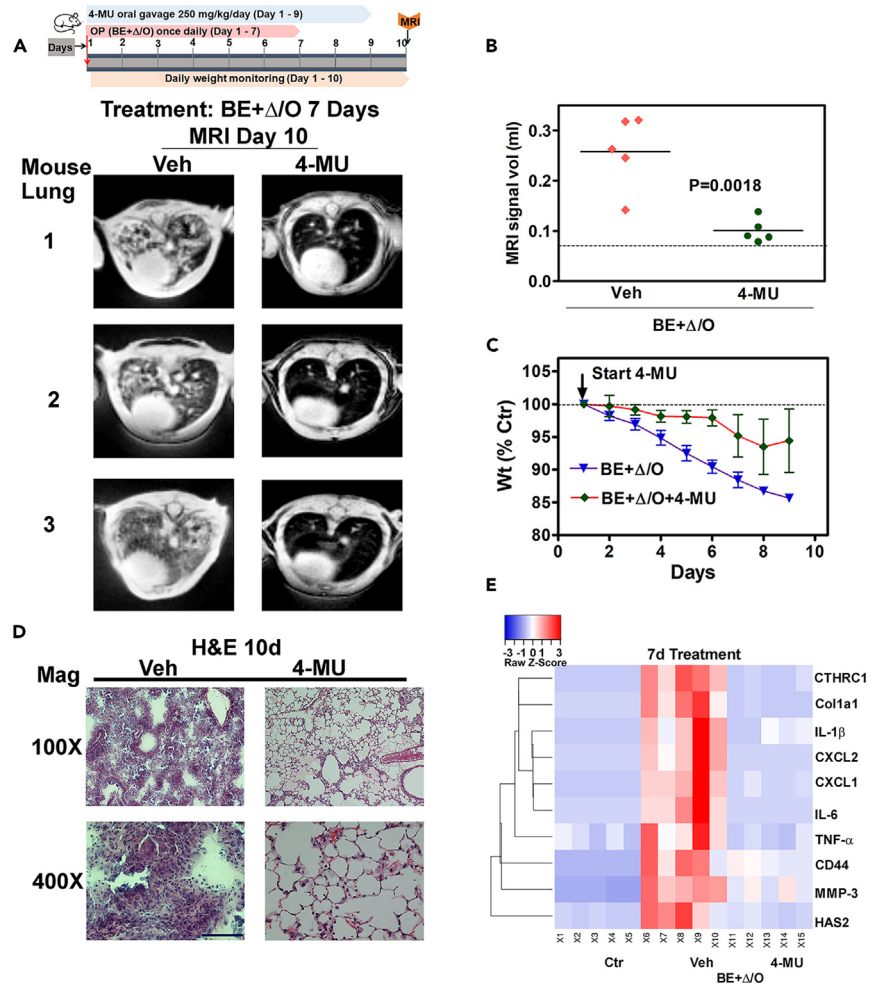
Figure 8. Evaluation of lung pathology in the BE + Delta OP model and of 4-MU treatment efficacy

As shown in the schematic, C57BL/6 mice received the oropharyngeal instillation of BE + Delta once daily for 7 days. Concurrently, mice were treated once daily with vehicle or 4-MU oral gavage until day 9. Mice were imaged by MRI on day ten, which was the experimental endpoint. n = 5 per group. The experimental endpoint was day ten, as the mice in the BE+Δ/O vehicle group became moribund and showed about 15% loss of body weight.

(A) MRI images of the lungs from three representative mice in each group on day ten.

(B) Quantification of the MRI signal from the lungs of mice in each group. Dots represent the MRI signal data for individual mice in each group; the line shows the mean intensity in each group.

(C) Body weights of mice in each group. The Y axis shows the percentage of mice weights compared to day 1 (100%) in each group. Data in B and C: Mean ± SD (n = 5 per group).

(D) Representative hematoxylin-Eosin images of lung tissues in different groups.

(E) Hierarchical clustering of the expression of the ten transcripts in mouse tissues from the control, vehicle, and 4-MU treatment groups. Transcript expression data are shown in Figure S8.

development of severe COVID-19 pathologies and associated morbidity. 4-MU did not cause a decrease in the basal levels of HA and HA-family in the lung tissues from the treatment groups, which is consistent with a previous report that 4-MU/4-MUG causes minimal decrease in the basal levels of HA in various tissues.[38,60] Furthermore, 4-MU treatment neither decreases leukocytes levels in tissues and in lymph nodes nor does it induce ROS production or loss of viability in leukocyte.[38,60] These findings establish the plausible therapeutic efficacy of 4-MU for COVID-19 with minimal toxicity.

A clinical study from China reported that 4-MU decreased disease progression in patients hospitalized for COVID-19.[19] While few details regarding the source of 4-MU (Hymecromone) and the trial design were provided, the study also reported that a single intratracheal instillation of HA (200–400 kD) in mice lungs caused ground opacities after four days.[19] The latter finding is surprising because HA polymers of various sizes (7–741 kD) are minimally retained in the lungs following intratracheal instillation.[61] Furthermore, high molecular mass HA (>215 kD) has a short retention time in the lungs (5–7 h).[61] A perceived conundrum regarding 4-MU's efficacy in various clinical and preclinical studies is its short half-life in circulation.[22] However, 4-MUG, also inhibits HA synthesis, and is converted to 4-MU in futile cycling.[38] Our data on
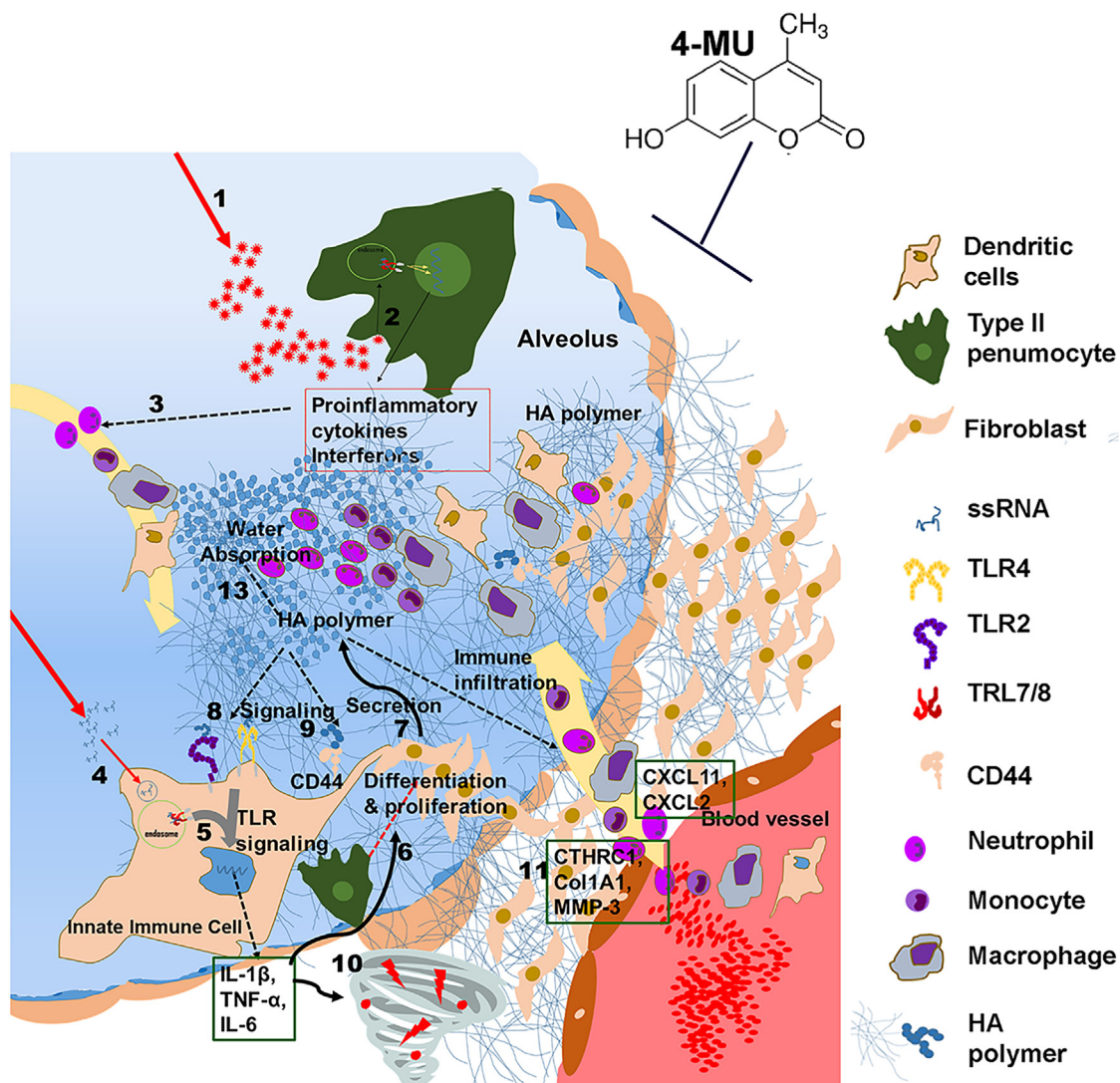
Figure 9. Schematic representation of HA induced COVID-19-like pathology and its inhibition by 4-MU
After the viral entry to the respiratory tract (1), SARS-CoV-2 mainly infects (2) alveolar type II pneumocytes through ACE2 receptors in the lower respiratory region. TLR7/8 receptors in the endosomes sense the SARS-CoV-2 ssRNA producing interferons and proinflammatory cytokines leading to (3) the infiltration of innate immune cells. Innate immune cells are primarily responsible for producing proinflammatory cytokines after (4) sensing the SARS-CoV-2 ssRNA or the ribo-oligonucleotides (CV2 or Δ/O). Low concentration of BE is introduced to facilitate inflammation to mimic virus induced inflammation and early immune activation. Innate immune cells produce proinflammatory cytokines through (5) TLR signaling which in turn results in the (6) differentiation and proliferation of type II pneumocytes. Fibroblasts along with type II pneumocytes and innate immune cells (7) actively secrete HA. (8) HA can engage TLR2 and TLR4 receptors to further activate TLR inflammatory signaling in the innate immune cells or signal through (9) HA-CD44 pathway in all cell types to activate inflammation and cellular differentiation and proliferation. The lack of clearance of pathogenic factors results in unregulated loop of innate activation and uncontrolled production of cytokines causing (10) cytokine storm. The effect of cytokine storm induces positive feedback loop onto the differentiation of type II pneumocytes to fibroblasts and proliferation and activation of interstitial fibroblasts which further enhances (11) collagen production and HA secretion in lungs. Moreover, (12) HA enhances immune cell infiltration into the interstitium and alveoli. (13) Due to its hygroscopic nature and water absorption property, high amount of HA production in lungs leads to pulmonary edema and ARDS. (14) 4-MU inhibits HA synthesis and blocks HA-induced inflammation and subsequent pathological manifestation.

the pharmacokinetics of 4-MU at a human equivalent dose of show high 4-MUG levels in the lungs even at 12 h, suggesting that oral 4-MU treatment would be effective even at a reduced dose.

In summary, our study demonstrates that the virus-free BE + CV2 and BE+(Δ/O) models mirror COVID-19 pathologies observed in patients. Furthermore, HA is a strong mediator of the severe pathological manifestations observed in patients with COVID-19 and that 4-MU has potential to effectively prevent and treat COVID-19 symptoms and PAC.

Limitations of the study

The following are the limitations of our study. First, because of technical restrictions, we could not estimate the amount of CV2 or the Δ/O ribo-oligonucleotide uptake in lung tissues following OP instillation and whether the ribo-oligonucleotides were preferentially taken up by certain cell types (e.g., alveolar cells). Second, we selected the ribo-oligonucleotides based on the selection criteria of >40% content of GU or UG pairs and at least one GUGU or UGUG motif. However, it is possible that other sequences in the SARS-COV-2 genome also generate lung pathologies that we observed in our models. Nevertheless, the design of the OP model described in this study may allow future research in this area. Third, the premise of the study was based on generating virus-free models, and therefore, the study did not include a side-be-side comparison with the live virus. However, the comparison of patient samples and lung tissues/extracts, MRI images, lung pathologies demonstrate that these animals models induce COVID-19-like pathologies. Lastly, in our studies we used a single dose of 4-MU based on the dose that is used for treating biliary spasms in patients. Nonetheless, our pharmacokinetics studies show that dose reduction is possible for the 4-MU oral treatment to prevent/inhibit COVID-19 and plausibly PAC.

STAR★METHODS

Detailed methods are provided in the online version of this paper and include the following:

- KEY RESOURCES TABLE
- RESOURCE AVAILABILITY
  - Lead contact
  - Materials availability
  - Data and code availability
- EXPERIMENTAL MODEL AND STUDY PARTICIPANT DETAILS
  - Ethical committee approval
- METHOD DETAILS
  - Specimens
  - Murine oropharyngeal (OP) aspiration model
  - Magnetic resonance imaging (MRI) imaging
  - HA ELISA-like assay (HA test)
  - Immunohistochemistry (IHC)
  - Immunocytochemistry
  - Real-time qPCR and immunoblot analyses
- QUANTIFICATION AND STATISTICAL ANALYSES

SUPPLEMENTAL INFORMATION

Supplemental information can be found online at https://doi.org/10.1016/j.isci.2024.109191.

AUTHOR CONTRIBUTIONS

H.Z., A.S., and K.A.: data curation, data interpretation, formal analysis, investigation, methodology, software, validation, visualization, and writing (review and editing); F.B., S.S., M.G., J.R., JVDE, and W.Z.: investigation and writing (review and editing); S.P.: validation and writing (review and editing); A.L., R.B., J.W., and M.T.: resources (specimen collection and processing) and writing (review and editing); N.P. and K.K.: data interpretation and writing (review and editing); B.L. and N.S.: conceptualization, investigation, methodology, resources, data interpretation, and writing (review and editing); V.L.: conceptualization, investigation, methodology, data interpretation, formal analysis, project administration, funding, supervision, resources, and writing (original draft, review, and editing).

DECLARATION OF INTERESTS

None.

REFERENCES

1. Mouffak, S., Shubbar, Q., Saleh, E., and El-Awady, R. (2021). Recent advances in management of COVID-19: A review. Biomed. Pharmacother. *143*, 112107. https://doi.org/10.1016/j.biopha.2021.112107.

2. Hashemian, S.M.R., Sheida, A., Taghizadieh, M., Memar, M.Y., Hamblin, M.R., Bannazadeh Baghi, H., Sadri Nahand, J., Asemi, Z., and Mirzaei, H. (2023). Paxlovid (Nirmatrelvir/Ritonavir): A new approach to Covid-19 therapy? Biomed. Pharmacother. *162*, 114367. https://doi.org/10.1016/j.biopha.2023.114367.

3. Fernandes, Q., Inchakalody, V.P., Merhi, M., Mestiri, S., Taib, N., Moustafa Abo El-Ella, D., Bedhiafi, T., Raza, A., Al-Zaidan, L., Mohsen, M.O., et al. (2022). Emerging COVID-19 variants and their impact on SARS-CoV-2 diagnosis, therapeutics and vaccines. Ann. Med. *54*, 524–540. https://doi.org/10.1080/07853890.2022.2031274.

4. Long, B., Carius, B.M., Chavez, S., Liang, S.Y., Brady, W.J., Koyfman, A., and Gottlieb, M. (2022). Clinical update on COVID-19 for the emergency clinician: Presentation and evaluation. Am. J. Emerg. Med. *54*, 46–57. https://doi.org/10.1016/j.ajem.2022.01.028.

5. Kumar, R., Srivastava, Y., Muthuramalingam, P., Singh, S.K., Verma, G., Tiwari, S., Tandel, N., Beura, S.K., Panigrahi, A.R., Maji, S., et al. (2023). Understanding Mutations in Human SARS-CoV-2 Spike Glycoprotein: A Systematic Review & Meta-Analysis. Viruses *15*, 856. https://doi.org/10.3390/v15040856.

6. Abdelnabi, R., Foo, C.S., Kaptein, S.J.F., Boudewijns, R., Vangeel, L., De Jonghe, S., Jochmans, D., Weynand, B., and Neyts, J. (2022). A SCID Mouse Model To Evaluate the Efficacy of Antivirals against SARS-CoV-2 Infection. J. Virol. *96*, e0075822. https://doi.org/10.1128/jvi.00758-22.

7. Battulin, N.R., and Serov, O.L. (2022). Creation of transgenic mice susceptible to coronaviruses: a platform for studying viral pathogenesis and testing vaccines. Vavilovskii Zhurnal Genet. Selektsii *26*, 402–408. https://doi.org/10.18699/VJGB-22-49.

8. Dinnon, K.H., 3rd, Leist, S.R., Okuda, K., Dang, H., Fritch, E.J., Gully, K.L., De la Cruz, G., Evangelista, M.D., Asakura, T., Gilmore, R.C., et al. (2022). SARS-CoV-2 infection produces chronic pulmonary epithelial and immune cell dysfunction with fibrosis in mice. Sci. Transl. Med. *14*, eabo5070. https://doi.org/10.1126/scitranslmed.abo5070.

9. Kant, R., Kareinen, L., Smura, T., Freitag, T.L., Jha, S.K., Alitalo, K., Meri, S., Sironen, T., Saksela, K., Strandin, T., et al. (2021). Common Laboratory Mice Are Susceptible to Infection with the SARS-CoV-2 Beta Variant. Viruses *13*, 2263. https://doi.org/10.3390/v13112263.

10. Bonaventura, A., Vecchié, A., Wang, T.S., Lee, E., Cremer, P.C., Carey, B., Rajendram, P., Hudock, K.M., Korbee, L., Van Tassell, B.W., et al. (2020). Targeting GM-CSF in COVID-19 pneumonia: rationale and strategies. Front. Immunol. *11*, 1625. https://doi.org/10.3389/fimmu.2020.01625.

11. Dentener, M.A., Vernooy, J.H.J., Hendriks, S., and Wouters, E.F.M. (2005). Enhanced levels of hyaluronan in lungs of patients with COPD: relationship with lung function and local inflammation. Thorax *60*, 114–119. https://doi.org/10.1136/thx.2003.020842.

12. Hellman, U., Karlsson, M.G., Engström-Laurent, A., Cajander, S., Dorofte, L., Ahlm, C., Laurent, C., and Blomberg, A. (2020). Presence of hyaluronan in lung alveoli in severe Covid-19: An opening for new treatment options? J. Biol. Chem. *295*, 15418–15422. https://doi.org/10.1074/jbc.AC120.015967.

13. Johnson, P., Arif, A.A., Lee-Sayer, S.S.M., and Dong, Y. (2018). Hyaluronan and Its Interactions With Immune Cells in the Healthy and Inflamed Lung. Front. Immunol. *9*, 2787. https://doi.org/10.3389/fimmu.2018.02787.

14. Albtoush, N., and Petrey, A.C. (2022). The role of hyaluronan synthesis and degradation in the critical respiratory illness COVID-19. Am. J. Physiol. Cell Physiol. *322*, C1037–C1046. https://doi.org/10.1152/ajpcell.00071.2022.

15. Marinho, A., Nunes, C., and Reis, S. (2021). Hyaluronic Acid: A Key Ingredient in the Therapy of Inflammation. Biomolecules *11*, 1518. https://doi.org/10.3390/biom11101518.

16. Jordan, A.R., Racine, R.R., Hennig, M.J.P., and Lokeshwar, V.B. (2015). The Role of CD44 in Disease Pathophysiology and Targeted Treatment. Front. Immunol. *6*, 182. https://doi.org/10.3389/fimmu.2015.00182.

17. Katoh, S. (2021). Critical Involvement of CD44 in T Helper Type 2 Cell-Mediated Eosinophilic Airway Inflammation in a Mouse Model of Acute Asthma. Front. Immunol. *12*, 811600. https://doi.org/10.3389/fimmu.2021.811600.

18. Chistyakov, D.V., Nikolskaya, A.I., Goriainov, S.V., Astakhova, A.A., and Sergeeva, M.G. (2020). Inhibitor of Hyaluronic Acid Synthesis 4-Methylumbelliferone as an Anti-Inflammatory Modulator of LPS-Mediated Astrocyte Responses. Int. J. Mol. Sci. *21*, 8203. https://doi.org/10.3390/ijms21218203.

19. Yang, S., Ling, Y., Zhao, F., Li, W., Song, Z., Wang, L., Li, Q., Liu, M., Tong, Y., Chen, L., et al. (2022). Hymecromone: a clinical prescription hyaluronan inhibitor for efficiently blocking COVID-19 progression. Signal Transduct. Target. Ther. *7*, 91. https://doi.org/10.1038/s41392-022-00952-w.

20. Kakizaki, I., Kojima, K., Takagaki, K., Endo, M., Kannagi, R., Ito, M., Maruo, Y., Sato, H., Yasuda, T., Mita, S., et al. (2004). A novel mechanism for the inhibition of hyaluronan biosynthesis by 4-methylumbelliferone. J. Biol. Chem. *279*, 33281–33289. https://doi.org/10.1074/jbc.M405918200.

21. Kultti, A., Pasonen-Seppänen, S., Jauhiainen, M., Rilla, K.J., Kärnä, R., Pyöriä, E., Tammi, R.H., and Tammi, M.I. (2009). 4-Methylumbelliferone inhibits hyaluronan synthesis by depletion of cellular UDP-glucuronic acid and downregulation of hyaluronan synthase 2 and 3. Exp. Cell Res. *315*, 1914–1923. https://doi.org/10.1016/j.yexcr.2009.03.002.

22. Nagy, N., Kuipers, H.F., Frymoyer, A.R., Ishak, H.D., Bollyky, J.B., Wight, T.N., and Bollyky, P.L. (2015). 4-methylumbelliferone treatment and hyaluronan inhibition as a therapeutic strategy in inflammation, autoimmunity, and cancer. Front. Immunol. *6*, 123. https://doi.org/10.3389/fimmu.2015.00123.

23. Arai, E., Nishida, Y., Wasa, J., Urakawa, H., Zhuo, L., Kimata, K., Kozawa, E., Futamura, N., and Ishiguro, N. (2011). Inhibition of hyaluronan retention by 4-methylumbelliferone suppresses osteosarcoma cells in vitro and lung metastasis in vivo. Br. J. Cancer *105*, 1839–1849. https://doi.org/10.1038/bjc.2011.459.

24. Yates, T.J., Lopez, L.E., Lokeshwar, S.D., Ortiz, N., Kallifatidis, G., Jordan, A., Hoye, K., Altman, N., and Lokeshwar, V.B. (2015). Dietary supplement 4-methylumbelliferone: an effective chemopreventive and therapeutic agent for prostate cancer. J. Natl. Cancer Inst. *107*, djv085. https://doi.org/10.1093/jnci/djv085.

25. Morera, D.S., Hennig, M.S., Talukder, A., Lokeshwar, S.D., Wang, J., Garcia-Roig, M., Ortiz, N., Yates, T.J., Lopez, L.E., Kallifatidis, G., et al. (2017). Hyaluronic acid family in bladder cancer: potential prognostic biomarkers and therapeutic targets. Br. J. Cancer *117*, 1507–1517. https://doi.org/10.1038/bjc.2017.318.

26. McKallip, R.J., Ban, H., and Uchakina, O.N. (2015). Treatment with the hyaluronic Acid synthesis inhibitor 4-methylumbelliferone suppresses LPS-induced lung inflammation. Inflammation *38*, 1250–1259. https://doi.org/10.1007/s10753-014-0092-y.

27. Galkina, S.I., Fedorova, N.V., Ksenofontov, A.L., Golenkina, E.A., Serebryakova, M.V., Stadnichuk, V.I., Baratova, L.A., and Sud'ina, G.F. (2022). Inhibitor of Hyaluronic Acid Synthesis 4-Methylumbelliferone Suppresses the Secretory Processes That Ensure the Invasion of Neutrophils into Tissues and Induce Inflammation. Biomedicines *10*, 314. https://doi.org/10.3390/biomedicines10020314.

28. Rosser, J.I., Nagy, N., Goel, R., Kaber, G., Demirdjian, S., Saxena, J., Bollyky, J.B., Frymoyer, A.R., Pacheco-Navarro, A.E., Burgener, E.B., et al. (2022). Oral hymecromone decreases hyaluronan in human study participants. J. Clin. Invest. *132*, e157983. https://doi.org/10.1172/JCI157983.

29. Heil, F., Hemmi, H., Hochrein, H., Ampenberger, F., Kirschning, C., Akira, S., Lipford, G., Wagner, H., and Bauer, S. (2004). Species-specific recognition of single-stranded RNA via toll-like receptor 7 and 8. Science *303*, 1526–1529. https://doi.org/10.1126/science.1093620.

30. Li, Y., Chen, M., Cao, H., Zhu, Y., Zheng, J., and Zhou, H. (2013). Extraordinary GU-rich single-strand RNA identified from SARS coronavirus contributes an excessive innate immune response. Microbes Infect. *15*, 88–95. https://doi.org/10.1016/j.micinf.2012.10.008.

31. Muppirala, U.K., Honavar, V.G., and Dobbs, D. (2011). Predicting RNA-protein interactions using only sequence information. BMC Bioinf. *12*, 489. https://doi.org/10.1186/1471-2105-12-489.

32. Moeller, A., Ask, K., Warburton, D., Gauldie, J., and Kolb, M. (2008). The bleomycin animal model: a useful tool to investigate treatment options for idiopathic pulmonary fibrosis? Int. J. Biochem. Cell Biol. *40*, 362–382. https://doi.org/10.1016/j.biocel.2007.08.011.

33. Grandi, A., Ferrini, E., Mecozzi, L., Ciccimarra, R., Zoboli, M., Leo, L., Khalajzeyqami, Z., Kleinjan, A., Löwik, C.W.G.M., Donofrio, G., et al. (2023). Indocyanine-enhanced mouse model of bleomycin-induced lung fibrosis with hallmarks of progressive emphysema. Am. J. Physiol. Lung Cell Mol. Physiol. *324*, L211–L227. https://doi.org/10.1152/ajplung.00180.2022.

34. Barbayianni, I., Ninou, I., Tzouvelekis, A., and Aidinis, V. (2018). Bleomycin Revisited: A

Direct Comparison of the Intratracheal Micro-Spraying and the Oropharyngeal Aspiration Routes of Bleomycin Administration in Mice. Front. Med. *5*, 269. https://doi.org/10.3389/fmed.2018.00269.

35. Egger, C., Cannet, C., Gérard, C., Jarman, E., Jarai, G., Feige, A., Suply, T., Micard, A., Dunbar, A., Tigani, B., and Beckmann, N. (2013). Administration of bleomycin via the oropharyngeal aspiration route leads to sustained lung fibrosis in mice and rats as quantified by UTE-MRI and histology. PLoS One *8*, e63432. https://doi.org/10.1371/journal.pone.0063432.

36. Borczuk, A.C., Salvatore, S.P., Seshan, S.V., Patel, S.S., Bussel, J.B., Mostyka, M., Elsoukkary, S., He, B., Del Vecchio, C., Fortarezza, F., et al. (2020). COVID-19 pulmonary pathology: a multi-institutional autopsy cohort from Italy and New York City. Mod. Pathol. *33*, 2156–2168. https://doi.org/10.1038/s41379-020-00661-1.

37. Bösmüller, H., Matter, M., Fend, F., and Tzankov, A. (2021). The pulmonary pathology of COVID-19. Virchows Arch. *478*, 137–150. https://doi.org/10.1007/s00428-021-03053-1.

38. Nagy, N., Gurevich, I., Kuipers, H.F., Ruppert, S.M., Marshall, P.L., Xie, B.J., Sun, W., Malkovskiy, A.V., Rajadas, J., Grandoch, M., et al. (2019). 4-Methylumbelliferyl glucuronide contributes to hyaluronan synthesis inhibition. J. Biol. Chem. *294*, 7864–7877. https://doi.org/10.1074/jbc.RA118.006166.

39. Ratna, S., Chiba, M., Bandyopadhyay, L., and Pang, K.S. (1993). Futile cycling between 4-methylumbelliferone and its conjugates in perfused rat liver. Hepatology *17*, 838–853.

40. Lokeshwar, V.B., Obek, C., Pham, H.T., Wei, D., Young, M.J., Duncan, R.C., Soloway, M.S., and Block, N.L. (2000). Urinary hyaluronic acid and hyaluronidase: markers for bladder cancer detection and evaluation of grade. J. Urol. *163*, 348–356. https://doi.org/10.1016/s0022-5347(05)68050-0.

41. Lokeshwar, V.B., Obek, C., Soloway, M.S., and Block, N.L. (1997). Tumor-associated hyaluronic acid: a new sensitive and specific urine marker for bladder cancer. Cancer Res. *57*, 773–777.

42. Yang, Y.M., Noureddin, M., Liu, C., Ohashi, K., Kim, S.Y., Ramnath, D., Powell, E.E., Sweet, M.J., Roh, Y.S., Hsin, I.F., et al. (2019). Hyaluronan synthase 2-mediated hyaluronan production mediates Notch1 activation and liver fibrosis. Sci. Transl. Med. *11*, eaat9284. https://doi.org/10.1126/scitranslmed.aat9284.

43. Kramer, M.W., Escudero, D.O., Lokeshwar, S.D., Golshani, R., Ekwenna, O.O., Acosta, K., Merseburger, A.S., Soloway, M., and Lokeshwar, V.B. (2011). Association of hyaluronic acid family members (HAS1, HAS2, and HYAL-1) with bladder cancer diagnosis and prognosis. Cancer *117*, 1197–1209. https://doi.org/10.1002/cncr.25565.

44. Almuntashiri, S., Zhang, D., Somanath, P.R., and Sikora, A. (2023). MMP3 in Severe COVID-19: A Biomarker or Therapeutic Target? Infect. Disord.: Drug Targets *23*, e190622206159. https://doi.org/10.2174/1871526522666220619121539.

45. Idota, M., Ishizuka, S., Hiraiwa, H., Yamashita, S., Oba, H., Kawamura, Y., Sakaguchi, T., Haga, T., Mizuno, T., Kawashima, I., et al. (2021). 4-Methylumbelliferone suppresses catabolic activation in anterior cruciate ligament-derived cells via a mechanism independent of hyaluronan inhibition. J. Orthop. Surg. Res. *16*, 507. https://doi.org/10.1186/s13018-021-02637-6.

46. Melms, J.C., Biermann, J., Huang, H., Wang, Y., Nair, A., Tagore, S., Katsyv, I., Rendeiro, A.F., Amin, A.D., Schapiro, D., et al. (2021). A molecular single-cell lung atlas of lethal COVID-19. Nature *595*, 114–119. https://doi.org/10.1038/s41586-021-03569-1.

47. Pérez-Mies, B., Caniego-Casas, T., Bardi, T., Carretero-Barrio, I., Benito, A., García-Cosío, M., González-García, I., Pizarro, D., Rosas, M., Cristóbal, E., et al. (2022). Progression to lung fibrosis in severe COVID-19 patients: A morphological and transcriptomic study in postmortem samples. Front. Med. *9*, 976759. https://doi.org/10.3389/fmed.2022.976759.

48. Calvert, B.A., Quiroz, E.J., Lorenzana, Z., Doan, N., Kim, S., Senger, C.N., Anders, J.J., Wallace, W.D., Salomon, M.P., Henley, J., and Ryan, A.L. (2023). Neutrophilic inflammation promotes SARS-CoV-2 infectivity and augments the inflammatory responses in airway epithelial cells. Front. Immunol. *14*, 1112870. https://doi.org/10.3389/fimmu.2023.1112870.

49. Zanza, C., Romenskaya, T., Manetti, A.C., Franceschi, F., La Russa, R., Bertozzi, G., Maiese, A., Savioli, G., Volonnino, G., and Longhitano, Y. (2022). Cytokine Storm in COVID-19: Immunopathogenesis and Therapy. Medicina (Kaunas) *58*, 144. https://doi.org/10.3390/medicina58020144.

50. Jyothula, S.S.K., Peters, A., Liang, Y., Bi, W., Shivshankar, P., Yau, S., Garcha, P.S., Yuan, X., Akkanti, B., Collum, S., et al. (2022). Fulminant lung fibrosis in non-resolvable COVID-19 requiring transplantation. EBioMedicine *86*, 104351. https://doi.org/10.1016/j.ebiom.2022.104351.

51. Wang, J., Jordan, A.R., Zhu, H., Hasanali, S.L., Thomas, E., Lokeshwar, S.D., Morera, D.S., Alexander, S., McDaniels, J., Sharma, A., et al. (2022). Targeting hyaluronic acid synthase-3 (HAS3) for the treatment of advanced renal cell carcinoma. Cancer Cell Int. *22*, 421. https://doi.org/10.1186/s12935-022-02818-1.

52. Babicki, S., Arndt, D., Marcu, A., Liang, Y., Grant, J.R., Maciejewski, A., and Wishart, D.S. (2016). Heatmapper: web-enabled heat mapping for all. Nucleic Acids Res. *44*, W147–W153. https://doi.org/10.1093/nar/gkw419.

53. Cao, W., Birkenbach, M., and Chen, S. (2022). Patterns of Inflammatory Cell Infiltration and Expression of STAT6 in the Lungs of Patients With COVID-19: An Autopsy Study. Appl. Immunohistochem. Mol. Morphol. *30*, 350–357. https://doi.org/10.1097/PAI.0000000000001023.

54. Hazeldine, J., and Lord, J.M. (2021). Neutrophils and COVID-19: Active Participants and Rational Therapeutic Targets. Front. Immunol. *12*, 680134. https://doi.org/10.3389/fimmu.2021.680134.

55. Lucas, F., and Sadigh, S. (2023). Hematopathology of Severe Acute Respiratory Syndrome Coronavirus 2 Infection and Coronavirus Disease-19. Surg. Pathol. Clin. *16*, 197–211. https://doi.org/10.1016/j.path.2023.01.007.

56. DeGrendele, H.C., Estess, P., Picker, L.J., and Siegelman, M.H. (1996). CD44 and its ligand hyaluronate mediate rolling under physiologic flow: a novel lymphocyte-endothelial cell primary adhesion pathway. J. Exp. Med. *183*, 1119–1130. https://doi.org/10.1084/jem.183.3.1119.

57. Lee-Sayer, S.S.M., Dong, Y., Arif, A.A., Olsson, M., Brown, K.L., and Johnson, P. (2015). The where, when, how, and why of hyaluronan binding by immune cells. Front. Immunol. *6*, 150. https://doi.org/10.3389/fimmu.2015.00150.

58. Ayilya, B.L., Balde, A., Ramya, M., Benjakul, S., Kim, S.K., and Nazeer, R.A. (2023). Insights on the mechanism of bleomycin to induce lung injury and associated in vivo models: A review. Int. Immunopharmacol. *121*, 110493. https://doi.org/10.1016/j.intimp.2023.110493.

59. Ferreira, N.D.R., Sanz, C.K., Raybolt, A., Pereira, C.M., and DosSantos, M.F. (2022). Action of Hyaluronic Acid as a Damage-Associated Molecular Pattern Molecule and Its Function on the Treatment of Temporomandibular Disorders. Front. Pain Res. *3*, 852249. https://doi.org/10.3389/fpain.2022.852249.

60. Nagy, N., Kaber, G., Johnson, P.Y., Gebe, J.A., Preisinger, A., Falk, B.A., Sunkari, V.G., Gooden, M.D., Vernon, R.B., Bogdani, M., et al. (2015). Inhibition of hyaluronan synthesis restores immune tolerance during autoimmune insulitis. J. Clin. Invest. *125*, 3928–3940. https://doi.org/10.1172/JCI79271.

61. Kuehl, C., Zhang, T., Kaminskas, L.M., Porter, C.J.H., Davies, N.M., Forrest, L., and Berkland, C. (2016). Hyaluronic Acid Molecular Weight Determines Lung Clearance and Biodistribution after Instillation. Mol. Pharm. *13*, 1904–1914. https://doi.org/10.1021/acs.molpharmaceut.6b00069.

STAR★METHODS

KEY RESOURCES TABLE

REAGENT or RESOURCE	SOURCE	IDENTIFIER
Antibodies		
Actin host Goat	Santa Cruz Biotechnology	sc-1615 HRP; Clone C11; Lot #J0914
HAS2 host Rabbit	Genescript	Custom synthesis; Affinity purified Polyclonal; Lot # 1
CD44 (HCAM) host Mouse	Santa Cruz Biotechnology	SC-7297 HRP; Clone DF1485; Lot #F0816
Collagen 1A1 (Col1A1) host Rabbit	Cell Signaling Technology	72026L; Clone E8F4L(XP®); Lot # 3
HA binding protein from Bovine cartilage (biotinylated)	In-house	Biotin HA binding protein
CD3 host Rabbit	Novus Biologicals	NB600-1441SS; Clone SP7; Lot #R230
CD68/SR-D1 host Rabbit	Novus Biologicals	MAB101141-SP; Clone 2449D; Lot # CMD1021021
Myeloperoxidase host Mouse	NSJ Bioreagents	V9354; Clone MPO/7118; Lot #V9354-21080
Mouse Ly6g/Gr1 host Rabbit	LS Bio	LS-C767966; polyclonal; Lot # 196857
CD44 host Rabbit	Cell Signaling	37259S; Clone E7K2Y; Lot # 3
Alexa Fluor® 594 AffiniPure Donkey Anti-Rabbit IgG (H + L)	Jacksonimmunoresearch	711-585-152
Alexa Fluor® 488 AffiniPure Donkey Anti-Mouse IgG (H + L)	Jacksonimmunoresearch	715-545-150
Biological samples		
Human adult bronchoalveolar lavage (BAL) specimens	This Study	N/A
Human adult postmortem lung tissue from patients with confirmed SARS-COV-2 infection	This Study	N/A
Chemicals, peptides, and recombinant proteins		
Bleomycin (sulfate) (0.125 mg/kg dose)	Cayman Chemical	13877
4-Methylumbelliferyl-β-D-glucuronide hydrate	Chemimpex	01410
4-Methylumbelliferone sodium salt	Millipore-Sigma	M1508
4-Methylumbelliferyl sulfate potassium salt	Millipore-Sigma	M7133
Critical commercial assays		
RNeasy™ Fibrous Tissue Mini Kit	Qiagen	74704
iScript™ cDNA Synthesis Kit	BioRad	1708891
SsoFast™ Evagreen Supermix	BioRad	1725204
DC™ Protein Assay	Bio Rad	5000111
Protease inhibitor cocktail	Millipore Sigma	P8340
Vectastain Elite ABC Kit, Peroxidase (Standard)	Vector Labs	PK-6100
Universal LSAB2 Kit/HRP	DAKO/Agilent	K060911-8
Liquid DAB+ Substrate Chromogen System	DAKO/Agilent	K3467 (K346711-2
Oligonucleotides		
CV2 5′rC*rG*rU*rG*rU*rA*rG* rA*rG*rU*rG*rU*rU*rU*rU*rU*rG-3′	Strain Wuhan	17202–17218 OM790279.1 nucleotides 17202 - 17218
Delta 5′rA*rA*rA*rC*rC*rU*rU*rG* rU*rA*rA*rU*rG*rG*rU*rG*rU*rU*rG-3′	Strain Delta	22871–22879 OK091006.1 nucleotides 22871–22879

(Continued on next page)

Continued		
REAGENT or RESOURCE	SOURCE	IDENTIFIER
Software and algorithms		
Graphpad Prism 8.0.0	Graphpad software	https://www.graphpad.com/
JMP Pro 14	JMP Pro software	https://www.jmp.com/
Other		
Cytoseal 60	Epredia	8310-4
Anti-Fade Fluorescence Mounting Medium	Abcam	AB104135
Protein block serum-free	DAKO/Agilient	X090930-2
Streptavidin, Alexa Fluor™ 488 conjugate	ThermoFisher	S11223
DAPI Invitrogen	ThermoFisher	D1306
Lipofectamin™ 3000 transfection reagent	ThermoFisher	L3000001

RESOURCE AVAILABILITY

Lead contact

Further information and requests should be directed to and will be fulfilled by the lead contact, Vinata B. Lokeshwar (vlokeshwar@augusta.edu).

Materials availability

The study generated Single strand (ss) RNA sequences in the Wuhan strain of SARS-COV-2 (CV2), and the B.1.617.2 lineage Delta/Omicron (Δ/O) variant. These ribo-oligonucleotides were synthesized with a phosphothioate bond modification by Integrated DNA Technologies. GenBank ID and sequence are available in the key resources table. Supplementary materials are available.

Data and code availability

All data reported in this paper can be made available upon reasonable request from the lead contact.

This paper does not report any original code.

Any additional information required to reanalyze the data reported in this paper is available from the lead contact upon request.

EXPERIMENTAL MODEL AND STUDY PARTICIPANT DETAILS

Ethical committee approval

This study was approved by the Augusta University Institutional Review Board (protocol # 1610562) in consultation with the Augusta University Environmental Health and Safety Office (BSP # 2014). The vertebrate animal experiments were conducted under a protocol approved by the Institutional Animal Use and Care Committee (AUP#2010–0201).

METHOD DETAILS

Specimens

Bronchoalveolar lavage (BAL) specimens from hospitalized patients were collected between December 2021 and January 2022. This study was approved by the Augusta University Institutional Review Board (protocol # 1610562) in consultation with the Augusta University Environmental Health and Safety Office (BSP # 2014). Postmortem lung tissue from patients with confirmed SARS-COV-2 infection who succumbed to hypoxic respiratory failure or other respiratory diseases were included in this study. Autopsies were performed after consent was obtained from next of kin. Use of human tissue for postmortem studies has been approved by the institutional review board (protocol # 611107); formalin-fixed COVID autopsy specimens were obtained under protocol # 1610562 designated for samples from SARS-COV-2 infected individuals between September 2020 and May 2022. All available patient characteristics for both cohorts are provided in Tables S3 and S5. The specimens were deidentified, delinked and demographic data regarding ethnicity, ancestry, or socioeconomic status were not available.

Murine oropharyngeal (OP) aspiration model

The vertebrate animal experiments were conducted under a protocol approved by the Institutional Animal Use and Care Committee (AUP#2010–0201). In each experiment, C57BL/6 mice in various groups (e.g., vehicle, 4-MU) were age matched and included both sexes, described as follows: Figure 1 groups: Ctr (4 Males, 1 Female; 2–5 months), BE (4 Males, 1 Female; 2–5 months), CV2 (2 Males, 3 Females; 3 months), BE + CV2 Veh (4 Males, 1 Female; 2–5 months), BE + CV2 4-MU (3 Males, 3 Females; 5 months). Figure 6 groups: BE + CV2

Veh (4 Males, 1 Female; 4–5 months), BE + CV2 4-MU (2 Males, 3 Females; 3–5 months). Figure 8 groups: BE+Δ/O Veh (4 Males, 1 Female; 4–5 months), BE+Δ/O 4-MU (2 Males, 3 Females; 3–5 months). Figure S7 group: BE + CV2 4-MU (3 males; 3–6 months).

CV2 or (Δ/O) ribo-oligonucleotide (10 μg/aspiration; 1 μg/μL stock) and Lipofectamin 3000 transfection reagent (10 μL) were mixed 1:1 in Dulbecco's Modified Eagles Medium. Bleomycin (BE; 0.125 mg/kg) was diluted in phosphate buffered saline (PBS). The oligo/lipofectamine mixture with or without BE, was placed onto the distal part of the oropharynx as described by Egger et al.[57] 4-MU or vehicle oral treatments were administered as per the experimental design described in each Figure. A decrease in body weight by 15% was the experimental endpoint, as approved under the AUP#2010–0201.

4-MU administration and pharmacokinetics (PK) of 4-MU in lung tissues by LC-MRM MS analysis: Mice received a daily gavage of vehicle (2% sucrose; 0.1 cc) or sodium salt of 4-MU (250 mg/kg) in 2% sucrose and euthanatized at different time intervals (0–24 h; n = 2 or 3/time point). Lung tissues (20 mg) was homogenized in PBS and 4-MU and metabolites were extracted in methyl *tert*-butyl ether. The clear upper phase was dried, reconstituted in methanol and separated on a Phenomenex Kinetex C18 column (100 × 2.1mm, 1.7um) using a Shimadzu Nexera UHPLC system and gradient elution from 20% to 90% acetonitrile (with 0.1% formic acid) in 5 min; flowrate of 0.2 mL/min. The eluent was ionized via negative ion electrospray on a TSQ Quantiva triple-quadrupole mass spectrometer (Thermo Scientific). The optimal collision energy levels and RF lens settings were determined using 4-MU and its metabolites, i.e., 4-methylumbelliferyl sulfate (4-MUS), 4-methylum-belliferyl-β-D-glucuronide (4-MUG), as standards (≥98% HPLC).

Magnetic resonance imaging (MRI) imaging

MRI images of mice lungs were recorded, individually in a BioSpec 70/20 USR MRI system with the following parameters: slice thickness = 1 mm; repetition time = 20 ms, echo time = 0.47 ms, flip angle = 15°, bandwidth = 200 kHz, 402 projections, 4 averages, matrix size = 128 × 128, field of view = 3.2 × 3.2 cm2; scan time: The total scan time per animal was 418 s. The Images (bright region) of whole lung from each mouse were quantified using the ImageJ software.

HA ELISA-like assay (HA test)

BAL specimens were heated at 700C for 20 min in 1% SDS-PBS solution and stored frozen at −800 C. For assaying, the samples were incubated in boiling water for 10 min and centrifugation at 14,000 rpm for 10 min.[39,58] HA levels in lung tissues and BAL specimens were measured by an ELISA-like assay and normalized to total protein levels.[39,58]

Immunohistochemistry (IHC)

Five-micron sections of paraffin-fixed tissues were placed on positively charged slides. The slides were made by the Electron Microscopy and Histology Core at Augusta University. The slides were sequentially deparaffinized, rehydrated and subjected to antigen retrieval by heating the slides at 95°C for 25 min in the Target-Retrieval Solution. The slides were then incubated with the primary antibodies; HA: DAKO antibody diluent 1:500; RT, 2h; HAS 2: 4% goat serum; 1:2000 RT, 2h; CD3: DAKO antibody diluent 1:100 40C O/N; CD68/SR-D1: DAKO antibody diluent 1:100 40C O/N; Myeloperoxidase: DAKO antibody diluent 1:200 40C O/N; Mouse Ly6g/Gr1: DAKO antibody diluent 1:500; RT, 2h; CD44: DAKO antibody diluent 1:200 40C O/N; Collagen 1A1 (Col1A1): DAKO antibody diluent 1:150 40C O/N. Primary antibodies are described in the key resources table. The slides were developed using the Dako LSAB kit and 3,3'-diaminobenzidine staining. Slide grading for staining intensity was performed by two individuals in a blinded fashion. To account for the heterogeneity in staining, each specimen was graded for staining intensity (0–3 +) and then multiplied by the area in the specimen staining, with that intensity (e.g., 25% × 0 = 0; 50% × 1+ = 50 and 25% × 2+ = 50). The intensity scores in all areas were added to obtain the staining score for the entire specimen (e.g., 0 + 50 + 50 = 100). Therefore, each specimen received a staining score between 0 and 300. The intensity scores of the two readers were then averaged to obtain the final score. Immune cells were counted at 400X magnification (high power field [HPF]).

Immunocytochemistry

Lung tissues were processed like the IHC procedure. Non-specific binding sites were blocked in 3% goat serum plus 1% bovine serum albumin solution followed by incubation with biotinylated HA-binding protein and a primary antibody. HA and the antigen (CD68, CD3 or Ly6G/mye-loperoxidase [MPO]) were visualized using Alexa Fluor 488 conjugated Streptavidin and Alexa Fluor 594 conjugated anti-rabbit antibody, respectively blocked with IF buffer: 1X PBS/1% BSA/0.3% Triton X-100 at 1:600 dilution. The images were acquired, and immune cells were counted using Keyence digital microscope under high-power-field.

Real-time qPCR and immunoblot analyses

Total RNA isolated from mouse lung tissues was subjected to quantitative RT-PCR using gene specific primers; primer sequences are provided in Table S6. For immunoblotting, tissues were homogenized in a non-ionic detergent solution, containing a protease inhibitor cocktail. The lysates were clarified by centrifugation and analyzed for specific proteins; actin was used as the loading control.

QUANTIFICATION AND STATISTICAL ANALYSES

All analyses in this study were performed using JMP Pro 14 and GraphPad Prism 8.0.0 software. Logistic regression single parameter analysis (univariate) was used to determine the association of HA levels with various parameters. Differences in MRI intensity signals, normalized

mRNA expression, HA levels, staining intensity or immune cell counts between two groups (vehicle versus 4-MU treatment) were analyzed by un-paired t-test or by Tukey's multiple comparison test for multiple group comparisons; p-values are two-tailed. For hierarchical clustering, a Z score was calculated for each sample based on the mean and SD of the expression of a transcript in all samples (i.e., control, vehicle, and 4-MU treatment). Z-scores were used for hierarchical clustering by centroid linkage and Euclidean distance measurement using the Heatmapper software (http://www.heatmapper.ca/).